Rapid Communications

Magnetic Weyl semimetals with diamond structure realized in spinel compounds

Wei Jiang,[1] Huaqing Huang,[2] Feng Liu,[2] Jian-Ping Wang,[1] and Tony Low[1,*]

[1]*Department of Electrical and Computer Engineering, University of Minnesota, Minneapolis, Minnesota 55455, USA*

[2]*Department of Materials Science and Engineering, University of Utah, Salt Lake City, Utah 84112, USA*

(Received 24 October 2019; accepted 6 March 2020; published 18 March 2020)

We discover an e_g-orbital (d_{z^2}, $d_{x^2-y^2}$) model within the diamond lattice (e_g-diamond model) that hosts novel topological states. Specifically, the e_g-diamond model yields a three-dimensional (3D) nodal cage (3D-NC), which is characterized by a d-d band inversion protected by two types of degenerate states (i.e., e_g-orbital and diamond-sublattice degeneracies). We demonstrate materials realization of this model in the well-known spinel compounds (AB_2X_4), where the tetrahedron-site cations (A) form the diamond sublattice. An ideal half metal with one metallic spin channel formed by well-isolated and half-filled e_g-diamond bands, accompanied by a large spin gap (4.36 eV) is discovered in one 4-2 spinel compound (VMg_2O_4), which becomes a magnetic Weyl semimetal when spin-orbit coupling effect is further considered. Our discovery greatly enriches the physics of diamond structure and spinel compounds, opening a door to their application in spintronics.

DOI: 10.1103/PhysRevB.101.121113

Quantum topological systems have attracted tremendous attention for both exotic physics (e.g., various quantum Hall effects [1,2], topological superconductivity [3], Weyl fermions [4]) and promising applications (e.g., spintronics [5] and quantum computing [6]). In particular, Weyl semimetal systems, characterized with momentum space separated monopole pairs, Fermi arc, and the chiral anomaly, have recently been explored extensively both experimentally and theoretically [7–15]. Magnetic Weyl semimetals have attracted special attention because of their intrinsic magnetic properties [15–21]. However, most of the studied Weyl semimetals have either both spin channels entangled near the Fermi level or Weyl points formed far away from the Fermi level [13,14], adding difficulties in studying the intrinsic properties of Weyl points. It is highly desirable if the Weyl points are located at the Fermi energy, allowing topological properties to be directly explored and exploited.

Studies of two-dimensional (2D) graphene have spawned various intriguing physical phenomena [22], such as Dirac fermion [23], quantum spin Hall effect [1], and superconductivity [24,25]. It has also stimulated many branches of exciting researches, such as silicene, germanene and its 2D analogs [26], valleytronics that utilize k and k' valley degree of freedom [27,28], and the $p_{x,y}$-orbital counterpart of graphene with flat band and Wigner crystallization [29,30]. The diamond structure, which is essentially formed by stacking buckled honeycomb layer in the A-B-C configuration, can be viewed as a three-dimensional (3D) analog of the 2D honeycomb lattice. It is the simplest system to study analogous exotic physics in three dimensions. Based on diamond structure, a theoretical proposal had indeed been made to achieve 3D topological insulators [31], whose proposal has yet been able to be mapped onto real materials. It would be important to identify a physical model based on diamond structure that spawns intriguing topological states and can be realized in real materials.

One of the most famous families of materials that hold the same group symmetry as diamond (Fd-$3m$) is the spinel compounds (AB_2O_4) [32–34]. With remarkable magnetic properties, spinel compounds have been extensively studied for decades for their promising applications, e.g., permanent magnets, power handling, and magnetic recording [35]. Surprisingly, its topological properties have been greatly overlooked [12], where only $HgCr_2Se_4$ has been proposed to be magnetic Weyl semimetal due to the band inversion between $|S\rangle$ and $|P\rangle$ states from Se [36]. Careful examinations show that there are several advantages studying topological properties of spinel compounds, including, for example, perfect diamond structure sublattice, good isolation of localized d orbitals for ideal band structure with clean topological features, versatility and high tunability, and mature materials synthesis.

Here, based on tight-binding analysis, we develop a novel two e_g-orbitals (d_{z^2} and $d_{x^2-y^2}$) model on the diamond structure (e_g-diamond model). When both nearest-neighbor (NN) and next-NN (NNN) interactions are considered, the e_g-diamond bands form a Dirac/Weyl nodal cage (NC) in the 3D Brillouin zone with hourglass fermions corresponding to the Dirac/Weyl points in the 2D case. The hourglass fermions involved are protected by the coexistence of e_g orbitals degeneracy and diamond crystal symmetry with A, B sublattices degeneracy. Furthermore, we demonstrate real materials realization of the model in a representative 4-2 spinel compound ($V^{4+}Mg_2^{2+}O_4$) using first-principles calculations. The spin-polarized e_g-diamond bands are exactly half-filled and isolated from other bands because of the strong tetrahedron crystal field splitting and the exchange splitting. The spin-orbit coupling effect further breaks the degeneracy of the 3D-NC, leading to the magnetic Weyl semimetal state. It is exciting to note that VMg_2O_4 has excellent lattice matching (and chemical compatibility) with MgO, which is a widely used spintronics oxide material in industry. This opens the

*Corresponding author. tlow@umn.edu

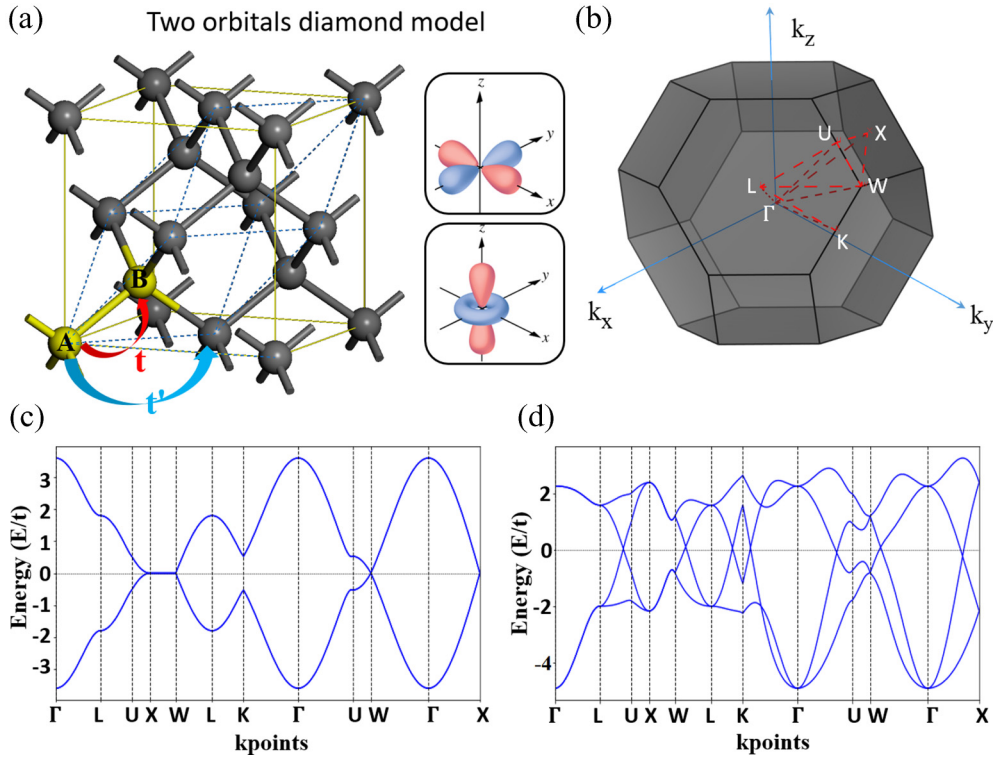

FIG. 1. Topological semimetal in the e_g-orbital diamond model. (a) Two-orbital diamond model with nearest-neighbor t and next-nearest-neighbor hopping t'. Insets show the d_{z^2} and $d_{x^2-y^2}$ orbitals for the given coordinates. (b) First-Brillouin zone with high-symmetry k points and k paths. (c) Tight-binding band structure of double degenerate single-orbital diamond model with only the NN hopping along high-symmetry paths shown in (b). (d) Tight-binding band structure of the e_g-diamond model with nonzero NNN hopping t', showing various linear crossing around the Fermi level.

door for the realization of novel spintronics devices, such as achieving low switching energy magnetic devices.

Tight-binding model. We first present here the 3D e_g-diamond model, different from the well-known sp^3- or sp^3s^*-diamond model. In the diamond structure with the fcc Bravais lattice, there are two equivalent atomic sites in a unit cell (blue dashed lines), labeled as A and B in Fig. 1(a). By choosing the coordinates in Fig. 1(a) as the orbital quantization axes, we select two energetically degenerate atomic $d_{x^2-y^2}$ and d_{z^2} orbitals (e_g orbitals due to local tetrahedral crystal field) on each site for the e_g-diamond model. Without including the spin degree of freedom, this e_g-diamond model can be essentially described by a four-band Hamiltonian. To succinctly demonstrate the physics, we limit our Hamiltonian to only the essential NN and NNN interactions, which can be written as

$$\mathcal{H} = \sum_i \epsilon_i d_i^\dagger d_i + \sum_{\langle i,j\rangle} t d_i^\dagger d_j + \sum_{\langle\langle i,j\rangle\rangle} t'_{ij} d_i^\dagger d_j + \text{H.c.}, \qquad (1)$$

where ϵ_i represents the on-site energy of state at the i site; $d_i^\dagger$ and d_i are the creation and annihilation operators of d electrons at the site i, respectively; and t and t' are the NN and NNN hoppings, respectively. In the diamond structure, each atom has 4 NNs and 12 NNNs. Given the strict orthogonality between the two e_g orbitals, NN hopping terms between d_{z^2} and $d_{x^2-y^2}$ are zero. Nonzero NN hopping terms are among d_{z^2} or $d_{x^2-y^2}$ orbitals, which have the same hopping amplitude t for e_g orbitals along four tetrahedron directions due to the geometric isotropic nature of those hoppings. A more extensive tight-binding model with parameters based on the Slater-Koster matrix also confirms these features [37].

In the absence of the NNN interactions, the same amplitude between hoppings among d_{z^2} orbitals and that among $d_{x^2-y^2}$ orbitals guarantees the double degeneracy of the bands. This can be understood as two copies of the single-orbital diamond model due to the degeneracy of two e_g orbitals on each site, as shown in Fig. 1(c) [37]. In the single-orbital diamond model, the same NN hopping amplitude enables the formation of Dirac nodal lines along the X-W path due to twofold rotation symmetries (C_2 axis along the x, y, and z directions through the A and B sites). It is straightforward that X-W and its inversion and rotational symmetric paths (four threefold rotation axes along the tetrahedral bond direction) will have the same degeneracy. It is important to emphasize that there exist two types of band degeneracies: type A is due to the degeneracy of e_g orbitals (d_{z^2} and $d_{x^2-y^2}$) and type B owing to the C_2 rotational symmetry in the single-orbital diamond Hamiltonian with degenerate A and B sites.

Next, NNN hopping interactions are included. There are two types of NNN hoppings, i.e., hoppings between d_{z^2} and $d_{x^2-y^2}$ orbitals (termed type I thereafter, t'_1), and hoppings among $d_{z^2}/d_{x^2-y^2}$ orbitals (termed type II thereafter, t'_2). Considering each single-orbital diamond Hamiltonian as one block, type-I hopping terms mix the two unit blocks with the off-diagonal interaction, and the type-II hopping terms act as on-site energy variation of the two blocks [37]. A detailed

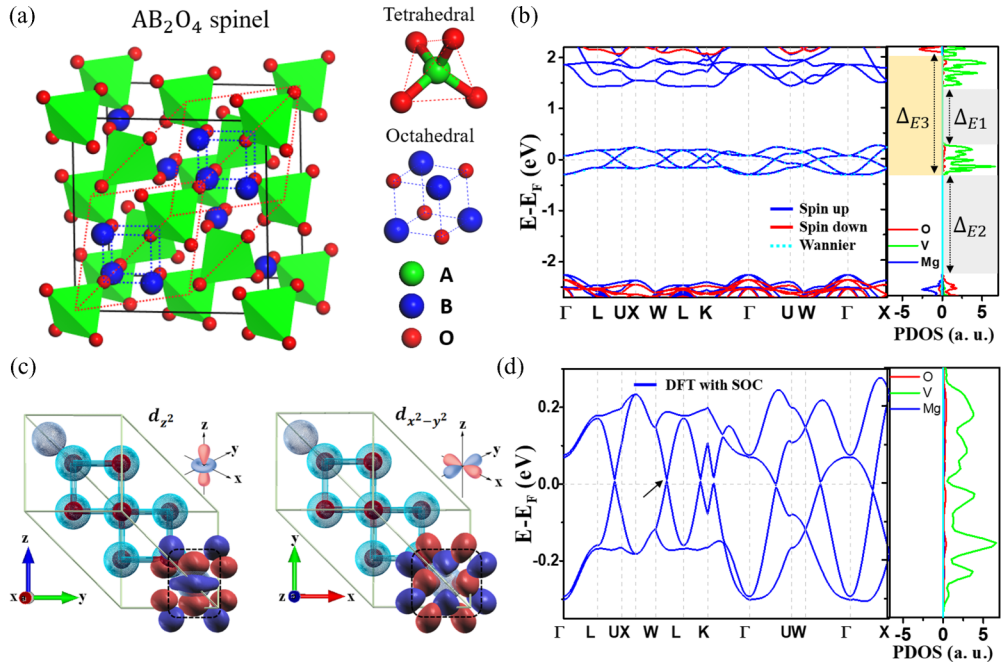

FIG. 2. Electronic and magnetic properties of VMg_2O_4. (a) Conventional atomic structure of an ionic spinel compound with chemical formula of AB_2O_4 with the primitive unit cell labeled using dashed red lines. Cations A and B occupy the tetrahedral and octahedral sites, respectively. (b) Band structure of 4-2 spinel ($V^{4+}Mg_2^{2+}O_4$), showing half-filled four-band structure isolated from the other bands with d-d crystal splitting gap Δ_{E1}, p-d charge transfer gap Δ_{E2}, and exchange splitting gap Δ_{E3}. Wannier fitted result is overlaid with cyan dotted lines. (c) Maximally localized Wannier functions of d_{z^2} and $d_{x^2-y^2}$ orbitals from Wannier fitting. (d) Enlarged four-band structure near the Fermi level from DFT considering SOC effect. The black arrow indicates the position of Weyl points.

analysis about the effects of these two hopping terms to the band structure can be found in the Supplemental Material [37]. Interestingly, we notice that under some symmetric hopping conditions, the band degeneracy along certain high-symmetry k paths remains even for nonzero t_1' and t_2' NNN hoppings.

Specifically, we find that at the center of the eight hexagonal Brillouin boundary (K_{HC}), the type-A degeneracy remains when the NNN hopping Hamiltonian keeps the C_4 rotational symmetry. Similarly, at the Γ and any point between Γ and K_{HC}, the band degeneracy remains while both C_4 rotational symmetry and the summation of hoppings along 12 NNN directions equals to zero [37]. Note the type-B degeneracy along the X-W path is also conserved as the C_2 rotation symmetry remains. One important outcome of the coexistence of two types of band degeneracy along different k paths is the guaranteed band crossing (nodal point, hourglass fermion) along certain k paths, where the two terminal k points have different types of degeneracies, as shown in Fig. 1(d). Such band crossing can be understood from the continuity nature of the wave functions that essentially leads to a d-d band inversion, since the two degenerate bands are formed with different orbital states [37]. As a consequence, those nodal points surprisingly construct a three-dimensional nodal cage, which will be further discussed later.

Magnetic semimetal in spinel compounds. To realize the aforementioned e_g-diamond model in real materials, we focus on the well-known spinel compounds that also have a space group of Fd-$3m$ as the diamond structure [32–34]. These inorganic oxides, with a chemical formula of AB_2O_4, are constructed by a fcc lattice of O^{2-} anions and interstitial cations in tetrahedral (T site) and octahedral (O site) sites formed by O^{2-} ions, as shown in Fig. 2(a). It is important to mention that in normal spinels, A cations in T sites form exactly a diamond structure and B cations in O sites form a 3D kagome lattice instead. To the best of our knowledge, though the diamond structure made by transition metal ions exists in many compounds, their intriguing electronic and topological properties have not been studied.

For A cations, the local tetrahedral crystal field splits five degenerate d orbitals into threefold degenerate t_{2g} and twofold degenerate e_g orbitals. Further exchange splitting of these d orbitals breaks the time-reversal symmetry and lifts the spin degeneracy [37]. With proper filling of e_g orbitals, e.g., one electron per site, half-filled magnetic e_g-diamond bands can be formed around the Fermi level. Indeed, we found one experimentally studied 4-2 spinel compound (VMg_2O_4) that perfectly satisfies these criteria [38,39], where vanadium cations ($4s^23d^3$) have one d electron left after donating four valence electrons (V^{4+}) to neighboring oxygen anions (O^{2-}). Our density functional theory calculations [37] show that VMg_2O_4 is ferromagnetic (FM) with a magnetic moment of $2\mu_B$ per unit cell, which are mainly contributed by V cations, as confirmed by the spin distribution plot [37]. The energy difference between the FM and the antiferromagnetic (AFM) state is around 0.43 eV at the Perdew-Burke-Ernzerhof (PBE) level, indicating a promising room temperature FM feature [37].

The band structure of VMg_2O_4 without considering the spin-orbit coupling (SOC) effect is shown in Fig. 2(b). There is a clear spin-polarized four-band structure right at the Fermi level with very good isolation from other bands. It exhibits

an ideal half-metallicity feature where one spin channel is metallic and the other spin channel is insulating with a band gap as large as 4.36 eV at the PBE level of accuracy. Further calculations using hybrid functionals show the same band structure with an even larger spin gap (5.17 eV for meta-GGA and 6.62 eV for Heyd-Scuseria-Ernzerhof [37]). To understand this peculiar electronic structure, we plotted and analyzed the projected density of states (PDOS) of VMg_2O_4. As shown in Fig. 2(b), the four bands around the Fermi level are nearly half-filled and mainly contributed by V d electrons, which agrees with the magnetic moment distribution. The PDOS of Mg are located far above the Fermi level, as the two valence electrons are fully transferred to O^{2-} ions to form the Mg^{2+} with zero valence electrons. The oxygen states are about 2 eV below the Fermi level because of the closed shell electronic configuration.

The observed band isolation in spin-up channel can be traced to the underlying energy splittings indicated as Δ_{E1} and Δ_{E2}, as shown in Fig. 2(b). The energy gap above (Δ_{E1}) is between d orbitals, which is essentially the tetrahedral crystal field splitting energy (Δ_{tet}) between e_g and t_{2g} orbitals. The large separation, $\Delta_{\text{tet}} \approx 2$ eV, is due to strong interactions with O^{2-} ions and the high oxidation state of V^{4+}. Δ_{E2} below the Fermi level is between d and p orbitals, which is the charge-transfer gap determined by the energy-level separation of orbitals between vanadium and oxygen. The separation can be well characterized by elemental electronegativity and the Madelung potential [40]. On the other hand, the large band gap in the spin-down channel can be understood as the cooperative effect of Δ_{E2} and Δ_{E3}. Δ_{E3} is essentially the exchange splitting of the V d electrons, which is known to be significant because of the strong localization effect of transition metal d orbitals. Ideally, such large gap would guarantee pure spin current and prevent any current leakage of the minority spin. To the best of our knowledge, this is also the largest spin gap among reported half-metallic ionic compounds.

E_g-diamond model and 3D-NC in VMg_2O_4. More interestingly, these four bands [Fig. 2(b)] have multiple linear crossings around the Fermi level, indicating a semimetallic feature. This is also supported by the enlarged PDOS plot, which shows nearly zero DOS around the Fermi level [Fig. 2(d)]. There also exist several degenerate bands along Γ-L, X-W, which agree perfectly with our e_g-diamond model. To confirm the e_g-diamond model, we performed the maximally localized Wannier functions (MLWFs) calculation to fit to the density functional theory (DFT) band structure using the WANNIER90 package [41]. The MLWFs fitted band structure based on two e_g orbitals on diamond lattice agrees perfectly with DFT results, as shown in Fig. 2(b). The calculated MLWFs show clearly the shape of d_{z^2} and $d_{x^2-y^2}$ orbitals [Fig. 2(c)], confirming the orbital characteristics and again validating the e_g-diamond model. This is further supported from the band-resolved partial charge distribution plot of these bands, which show a characteristic shape composed of the two orbitals [37].

As demonstrated from the e_g-diamond model, we expect the band structure of VMg_2O_4 to form a nodal cage in the first-Brillouin zone. To confirm the 3D-NC feature, we calculated the 3D band structures in two 2D k planes with one at the hexagonal Brillouin boundary [(111) surface, Fig. 3(a)] and the other one at k_x-k_y plane across the Γ point [(110) surface, Fig. 3(c)]. The 3D band structure [37] and the band-gap plot between the middle two Dirac bands [Figs. 3(b) and 3(d)] show clearly nodal ring features within both the hexagon (111) and octagon (110) planes. Based on the C_4 rotational and the inversion symmetry, the other seven hexagonal Brillouin zone boundaries also possess the same feature as the (111) surface [37]. Similarly, the same rules apply to symmetry invariant planes of the (110) surface, i.e., (101) and (011) planes across the Γ point due to the C_3 rotational symmetry [37].

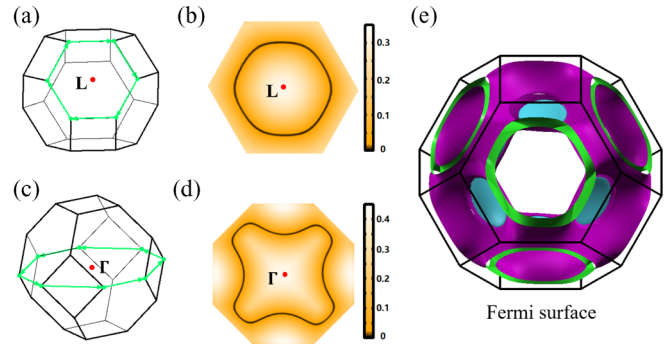

FIG. 3. 3D Nodal cage. (a) 2D hexagonal k plane of the (111) surface at the Brillouin zone edge. (b) Band gap between the middle two bands for the 2D k plane in (a). (c) and (d) same as (a) and (b) for the 2D octagonal k plane of the (110) surface across the Γ point of the 3D Brillouin zone. (e) Fermi surface at the energy of Fermi level, showing the feature of 3D nodal cage. Purple and blue regions represent the hole and electron pockets, respectively. Green region highlights the cross section at the Brillouin zone boundary.

From the band structure in Fig. 2(b), we noticed nearly all the nodal points are located closely adjacent to the Fermi level (<20 meV). Therefore, the Fermi surface could essentially capture the 3D-NC feature. Indeed, the Fermi surface plot, as shown in Fig. 3(e), shows a smooth surface that ends at the hexagonal Brillouin zone boundaries. Small energy dispersion of the 3D-NC leads to the coexistence of electron and hole pockets, where hole pockets are mostly located near square zone boundaries. Cross sections of the 3D Fermi/nodal cage for different planes (2D Fermi surface [37]) show that the nodal ring within the (111) surface is nearly flat, while that of the (110) surface shows small energy oscillation (± 20 meV) as it cut across the square zone boundaries. We also calculated the 3D band structure and 2D Fermi surface for two series of 2D k planes, i.e., (111) planes and (110) planes from the boundary to the center of the Brillouin zone, which further confirm the intriguing 3D-NC feature [37].

Magnetic Weyl semimetal. Generally, such nodal cage is not robust, which will become gapped after considering the SOC effect [42,43]. Depending on whether the system becomes fully gapped or not, the material becomes the quantum anomalous Hall insulator or magnetic Weyl semimetal. Therefore, we proceed to include the SOC to determine the topological phases of VMg_2O_4. Firstly, we performed noncollinear calculations with different spin configurations [37], which show that the system remains to be FM with nearly degenerate

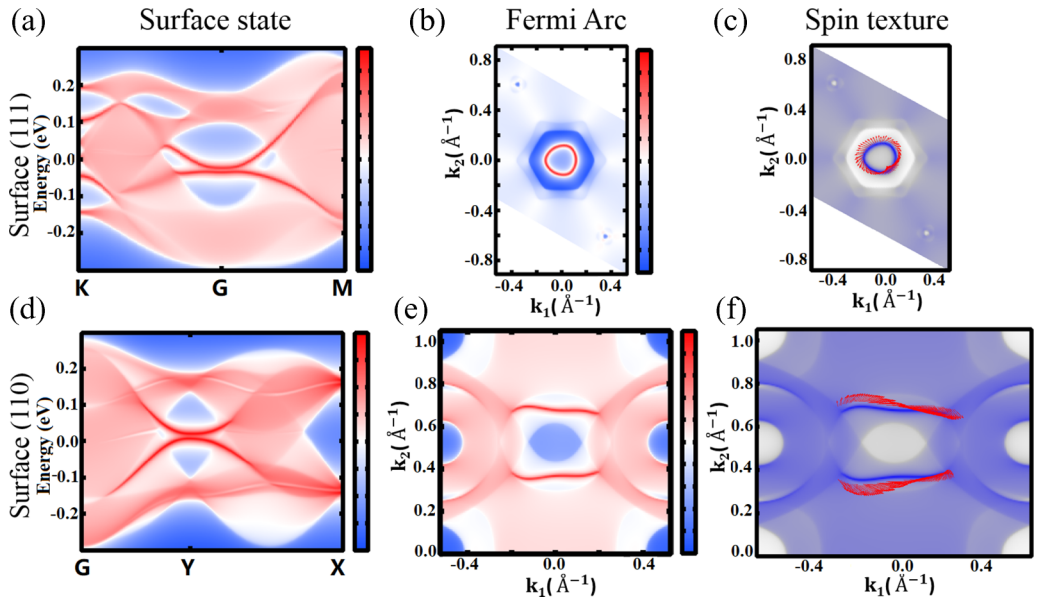

FIG. 4. Topological properties of Weyl semimetal VMg_2O_4. (a) Topological surface state connecting bulk states for the (111) surface. (b),(c) Fermi arc and the corresponding spin texture of the (111) surface. (d)–(f) Same as (a), (b), and (c) for the (110) surface.

energies along different magnetization directions. The corresponding band structure for the magnetization direction along the ⟨111⟩ direction is plotted along high-symmetry k paths [Fig. 2(d)], where most of the NC become gapped with several k points remaining degenerate, such as that along Γ-W that is perpendicular to the magnetic field. Detailed calculations show 18 Weyl pairs, as confirmed by the Berry phase of $\pm\pi$ through the Berry curvature integration around these points [37].

To demonstrate topological properties of VMg_2O_4, we calculated the surface state using a semi-infinite system based on the Green's function. Figures 4(a) and 4(d) show clearly topological surface states connecting bulk states for the (111) and (110) surfaces, respectively. As one of the characteristic features of Weyl semimetals, Fermi arcs for these two surfaces are also calculated, as shown in Figs. 4(b) and 4(e). The Fermi arcs show a dramatic difference between different surfaces due to different projections of Weyl pairs. For the (110) surface, two pairs of Weyl points can be clearly seen from the two separated Fermi arcs as required by the C_2 rotational symmetry. For the (111) surface, the Fermi arcs form a "Fermi ring" with three pairs of Weyl points due to the C_3 rotational symmetry. These Weyl points are accidentally overlapping while projecting to the (111) surface, which are separated within the bulk Brillouin zone. Spin textures of the Fermi arc shown in Figs. 4(c) and 4(f) also confirm the positive and negative chirality of Weyl points.

Discussion and perspectives. One of the intriguing properties of Weyl semimetals is their proposed large intrinsic anomalous Hall conductivity σ_H^A, which comes from the integration of Berry curvature from bulk band structure [44,45]. Considering the small charge current σ due to the semimetallic feature, it is believed that Weyl semimetals could have a large anomalous Hall angle σ_H^A/σ. Therefore, we calculated intrinsic anomalous Hall conductivity of VMg_2O_4, which shows a relatively large peak ($\approx 100\ \Omega^{-1}\,\mathrm{cm}^{-1}$) around the Fermi level [37]. Theoretical proposals suggest engineering extra bulk bands to cross the Fermi level may help to increase σ_H^A [46]. To test this idea, we modified the band dispersion through strain engineering and successfully realize the proposed band structure upon compressive strain. The σ_H^A indeed shows a large enhancement by at least twofold [37].

The intriguing phenomenon observed in VMg_2O_4 can also be extended to other spinel compounds. Through theoretical calculations, we find spinel compounds formed with elements having the same valance states as VMg_2O_4, e.g., VMg_2Se_4 and VCa_2O_4, share the same features as VMg_2O_4 [37]. On the other hand, based on the same model with different electron filling, some other potentially interesting phases can be realized with elements having different valence states. For example, we can acquire a large gap (≈ 3 eV) half-metal phase in $MnMg_2O_4$ and realize an FM insulating state in $CrMg_2O_4$ [37]. It is interesting to mention that the FM insulator possesses two different band gaps (0.6 and 3.6 eV) in different spin channels, which could potentially be used as a spin filter in magnetic tunneling junction devices.

On the other hand, the lattice compatibility/match with the (001) textured MgO tunneling barrier is critical for practical applications. Many materials, such as Heusler materials, that have been studied face practical integration issues with MgO because of lattice mismatch. Interestingly, the material we studied here has a very small lattice mismatch with MgO for both (001) and (111) planes ($<0.4\%$), because of their structural similarity [37]. This lattice matching might facilitate high-quality growth of VMg_2O_4 directly on top of MgO to study or utilize its intriguing magnetic Weyl semimetal features. For example, we can build magnetic tunnel junction devices with VMg_2O_4/MgO/VMg_2O_4 stacking or simply use VMg_2O_4 as the spin filtering layer [37].

In summary, we have discovered an e_g-diamond model which spawns an intriguing nodal cage feature due to the coexistence of orbital and sublattice degeneracies. We discovered that such model can be realized in the well-studied spinel

oxide compounds. Using the 4-2 spinel compound VMg_2O_4 as a representative example, we confirmed the validity of the e_g-diamond model and demonstrate the formation of 3D-NC due to linear crossing between the middle two bands. The material is calculated to be a magnetic Weyl semimetal, which is novel to spinel compounds. We further expand the model to a series of spinel compounds and demonstrate their promising applications as spintronic materials. This theoretical discovery substantially enriches the physics of spinel compounds and could potentially lead to new applications.

Acknowledgments. This project is supported by SMART, one of seven centers of nCORE, a Semiconductor Research Corporation program, sponsored by National Institute of Standards and Technology (NIST).

[1] C. L. Kane and E. J. Mele, Phys. Rev. Lett. **95**, 226801 (2005).
[2] M. Z. Hasan and C. L. Kane, Rev. Mod. Phys. **82**, 3045 (2010).
[3] X.-L. Qi and S.-C. Zhang, Rev. Mod. Phys. **83**, 1057 (2011).
[4] B. Yan and C. Felser, Annu. Rev. Condens. Matter Phys. **8**, 337 (2017).
[5] D. Pesin and A. H. MacDonald, Nat. Mater. **11**, 409 (2012).
[6] J. Moore, Nat. Phys. **5**, 378 (2009).
[7] A. A. Burkov and L. Balents, Phys. Rev. Lett. **107**, 127205 (2011).
[8] S.-Y. Xu, I. Belopolski, N. Alidoust, M. Neupane, G. Bian, C. Zhang, R. Sankar, G. Chang, Z. Yuan, C.-C. Lee, S.-M. Huang, H. Zheng, J. Ma, D. S. Sanchez, B. Wang, A. Bansil, F. Chou, P. P. Shibayev, H. Lin, S. Jia, and M. Z. Hasan, Science **349**, 613 (2015).
[9] B. Q. Lv, H. M. Weng, B. B. Fu, X. P. Wang, H. Miao, J. Ma, P. Richard, X. C. Huang, L. X. Zhao, G. F. Chen, Z. Fang, X. Dai, T. Qian, and H. Ding, Phys. Rev. X **5**, 031013 (2015).
[10] C. Shekhar, A. K. Nayak, Y. Sun, M. Schmidt, M. Nicklas, I. Leermakers, U. Zeitler, Y. Skourski, J. Wosnitza, Z. Liu, Y. Chen, W. Schnelle, H. Borrmann, Y. Grin, C. Felser, and B. Yan, Nat. Phys. **11**, 645 (2015).
[11] X. Wan, A. M. Turner, A. Vishwanath, and S. Y. Savrasov, Phys. Rev. B **83**, 205101 (2011).
[12] G. Xu, H. Weng, Z. Wang, X. Dai, and Z. Fang, Phys. Rev. Lett. **107**, 186806 (2011).
[13] C. Felser, L. Wollmann, S. Chadov, G. H. Fecher, and S. S. P. Parkin, APL Mater. **3**, 041518 (2015).
[14] Z. Wang, M. G. Vergniory, S. Kushwaha, M. Hirschberger, E. V. Chulkov, A. Ernst, N. P. Ong, R. J. Cava, and B. A. Bernevig, Phys. Rev. Lett. **117**, 236401 (2016).
[15] E. Liu, Y. Sun, N. Kumar, L. Muechler, A. Sun, L. Jiao, S.-Y. Yang, D. Liu, A. Liang, Q. Xu, J. Kroder, V. Süß, H. Borrmann, C. Shekhar, Z. Wang, C. Xi, W. Wang, W. Schnelle, S. Wirth, Y. Chen, S. T. B. Goennenwein, and C. Felser, Nat. Phys. **14**, 1125 (2018).
[16] D. F. Liu, A. J. Liang, E. K. Liu, Q. N. Xu, Y. W. Li, C. Chen, D. Pei, W. J. Shi, S. K. Mo, P. Dudin, T. Kim, C. Cacho, G. Li, Y. Sun, L. X. Yang, Z. K. Liu, S. S. P. Parkin, C. Felser, and Y. L. Chen, Science **365**, 1282 (2019).
[17] N. Morali, R. Batabyal, P. K. Nag, E. Liu, Q. Xu, Y. Sun, B. Yan, C. Felser, N. Avraham, and H. Beidenkopf, Science **365**, 1286 (2019).
[18] I. Belopolski, K. Manna, D. S. Sanchez, G. Chang, B. Ernst, J. Yin, S. S. Zhang, T. Cochran, N. Shumiya, H. Zheng, B. Singh, G. Bian, D. Multer, M. Litskevich, X. Zhou, S.-M. Huang, B. Wang, T.-R. Chang, S.-Y. Xu, A. Bansil, C. Felser, H. Lin, and M. Z. Hasan, Science **365**, 1278 (2019).
[19] S. Chowdhury, K. F. Garrity, and F. Tavazza, npj Comput. Mater. **5**, 33 (2019).
[20] S. Borisenko, D. Evtushinsky, Q. Gibson, A. Yaresko, K. Koepernik, T. Kim, M. Ali, J. v. d. Brink, M. Hoesch, A. Fedorov, E. Haubold,, Y. Kushnirenko, I. Soldatov, R. Schäfer, and R. J. Cava, Nat. Commun. **10**, 3424 (2019).
[21] A. Pertsova, R. M. Geilhufe, M. Bremholm, and A. V. Balatsky, Phys. Rev. B **99**, 205126 (2019).
[22] A. H. Castro Neto, F. Guinea, N. M. R. Peres, K. S. Novoselov, and A. K. Geim, Rev. Mod. Phys. **81**, 109 (2009).
[23] K. S. Novoselov, A. K. Geim, S. V. Morozov, D. Jiang, M. I. Katsnelson, I. V. Grigorieva, S. V. Dubonos, and A. A. Firsov, Nature (London) **438**, 197 (2005).
[24] B. Uchoa and A. H. Castro Neto, Phys. Rev. Lett. **98**, 146801 (2007).
[25] Y. Cao, V. Fatemi, S. Fang, K. Watanabe, T. Taniguchi, E. Kaxiras, and P. Jarillo-Herrero, Nature (London) **556**, 43 (2018).
[26] P. Vogt, P. De Padova, C. Quaresima, J. Avila, E. Frantzeskakis, M. C. Asensio, A. Resta, B. Ealet, and G. Le Lay, Phys. Rev. Lett. **108**, 155501 (2012).
[27] D. Gunlycke and C. T. White, Phys. Rev. Lett. **106**, 136806 (2011).
[28] Y. Jiang, T. Low, K. Chang, M. I. Katsnelson, and F. Guinea, Phys. Rev. Lett. **110**, 046601 (2013).
[29] C. Wu, D. Bergman, L. Balents, and S. Das Sarma, Phys. Rev. Lett. **99**, 070401 (2007).
[30] W. Jiang, Z. Liu, J.-W. Mei, B. Cui, and F. Liu, Nanoscale **11**, 955 (2019).
[31] L. Fu, C. L. Kane, and E. J. Mele, Phys. Rev. Lett. **98**, 106803 (2007).
[32] D. S. McClure, J. Phys. Chem. Solids **3**, 311 (1957).
[33] P. K. Baltzer, H. W. Lehmann, and M. Robbins, Phys. Rev. Lett. **15**, 493 (1965).
[34] K. E. Sickafus, J. M. Wills, and N. W. Grimes, J. Am. Ceram. Soc. **82**, 329 (1999).
[35] R. Valenzuela, Phys. Res. Int. **2012**, 591839 (2012).
[36] J. Zou, Z. He, and G. Xu, npj Comput. Mater. **5**, 96 (2019).
[37] See Supplemental Material at http://link.aps.org/supplemental/10.1103/PhysRevB.101.121113 for methods, tight-binding analysis, Curie temperature analysis, band formation, and non-collinear spin analysis.
[38] H. Oshima, S. Shirasaki, and H. Yamamura, J. Am. Ceram. Soc. **60**, 277 (1977).
[39] J. R. Hellmann and V. S. Stubican, J. Am. Ceram. Soc. **66**, 265 (1983).
[40] Y. Ohta, T. Tohyama, and S. Maekawa, Phys. Rev. Lett. **66**, 1228 (1991).
[41] N. Marzari and D. Vanderbilt, Phys. Rev. B **56**, 12847 (1997).
[42] H. Huang, W. Jiang, K.-H. Jin, and F. Liu, Phys. Rev. B **98**, 045131 (2018).

[43] H. Chen, S. Zhang, W. Jiang, C. Zhang, H. Guo, Z. Liu, Z. Wang, F. Liu, and X. Niu, J. Mater. Chem. A **6**, 11252 (2018).

[44] C. Zeng, Y. Yao, Q. Niu, and H. H. Weitering, Phys. Rev. Lett. **96**, 037204 (2006).

[45] S. Onoda, N. Sugimoto, and N. Nagaosa, Phys. Rev. Lett. **97**, 126602 (2006).

[46] E. Derunova, Y. Sun, C. Felser, S. S. P. Parkin, B. Yan, and M. N. Ali, Sci. Adv. **5**, eaav8575 (2019).